



Article

Chromatin Organization after High-LET Irradiation Revealed by Super-Resolution STED Microscopy

Benjamin Schwarz [†], Nicole Matejka, Sarah Rudigkeit, Matthias Sammer and Judith Reindl ^{*,†} 

Section Biomedical Radiation Physics, Institute for Applied Physics and Measurement Technology, Department for Aerospace Engineering, Universität der Bundeswehr München, 85577 Neubiberg, Germany

* Correspondence: judith.reindl@unibw.de; Tel.: +49-89-6004-4443

[†] These authors contributed equally to this work.

Abstract: Ion-radiation-induced DNA double-strand breaks can lead to severe cellular damage ranging from mutations up to direct cell death. The interplay between the chromatin surrounding the damage and the proteins responsible for damage recognition and repair determines the efficiency and outcome of DNA repair. The chromatin is organized in three major functional compartments throughout the interphase: the chromatin territories, the interchromatin compartment, and the perichromatin lying in between. In this study, we perform correlation analysis using super-resolution STED images of chromatin; splicing factor SC35, as an interchromatin marker; and the DNA repair factors 53BP1, Rad51, and γ H2AX in carbon-ion-irradiated human HeLa cells. Chromatin and interchromatin overlap only in protruding chromatin branches, which is the same for the correlation between chromatin and 53BP1. In contrast, between interchromatin and 53BP1, a gap of (270 ± 40) nm is visible. Rad51 shows overlap with decondensed euchromatic regions located at the borders of condensed heterochromatin with further correlation with γ H2AX. We conclude that the DNA damage is repaired in decondensed DNA loops in the perichromatin, located in the periphery of the DNA-dense chromatin compartments containing the heterochromatin. Proteins like γ H2AX and 53BP1 serve as supporters of the chromatin structure.

Keywords: chromatin organization; DNA repair; super-resolution microscopy; interchromatin; perichromatin



Citation: Schwarz, B.; Matejka, N.; Rudigkeit, S.; Sammer, M.; Reindl, J. Chromatin Organization after High-LET Irradiation Revealed by Super-Resolution STED Microscopy. *Int. J. Mol. Sci.* **2024**, *25*, 628. <https://doi.org/10.3390/ijms25010628>

Academic Editors: Salvatore Saccone and Marco Biggiogera

Received: 28 November 2023

Revised: 15 December 2023

Accepted: 27 December 2023

Published: 3 January 2024



Copyright: © 2024 by the authors. Licensee MDPI, Basel, Switzerland. This article is an open access article distributed under the terms and conditions of the Creative Commons Attribution (CC BY) license (<https://creativecommons.org/licenses/by/4.0/>).

1. Introduction

Ionizing radiation damages living cells by the ionization of the DNA molecule itself or by the induction of reactive species that then damage the DNA molecule. Depending on the type of radiation, the amount and type of damage vary. Overall, this damage can influence the survival capacity of cells or induce carcinogenesis. The most severe of the damage is the DNA double-strand break (DSB). If the repair of this damage is defective, it leads to genetic alterations, which can then directly lead to cell death or carcinogenetic mutations. Therefore, mammalian cells have developed a multitude of response mechanisms to DSBs. The most studied ones are the signal cascades leading to repair protein accumulation and different pathways to the repair of the damage. One of the most important reactions to radiation damage is the phosphorylation of the histone variant H2AX at serine 139, forming γ H2AX. This is mediated by the kinases ATM, ATR, and DNA-PK [1] in mega-base-pair (Mbp) large chromatin regions around the damage [2,3]. The γ H2AX can be labeled using antibodies, which makes it visible as ionizing-radiation-induced foci (IRIF) in microscopy. Upon detection of the DSB, repair starts. It is well accepted that the repair pathway choice is crucially dependent on the DNA replication status and the complexity of damage [4]. The major pathways are homologous recombination (HR) and non-homologous end-joining (NHEJ). The first needs to rely on the sister chromatin as a template, and the second only uses end processing and ligation of ends and is therefore independent of the cell

cycle. But with the discovery that each DSB is processed separately [5], more and more repair mechanisms lying somewhere between HR and NHEJ are discovered. It is assumed that the DNA end resection serves as a decisive step toward the type of repair [4]. The repair is mediated by a variety of proteins showing specific functions throughout the repair. Some are directly localized at the damage, but others cover a similar region to that of γ H2AX. Also, the function can be limited to only a specific step in one repair pathway or more general during the complete repair process. Rad51, for example, is a relevant protein in homologous recombination that binds directly at the location of the resected DNA. It forms small helical scaffolds, which support the single-stranded DNA (ssDNA) ends [6]; this facilitates the homology search [7,8]. By labeling Rad51, the ssDNA can be visualized, and the direct damage location can be identified using fluorescence microscopy [9,10]. A protein binding in the Mbp large regions, where also γ H2AX is formed, is 53BP1. 53BP1 is an early responder to DSB induction and is activated through ATM independent of the repair mechanism [11–15], where the active function of 53BP1 can only be verified through NHEJ [16]. In homology-dependent repair mechanisms, it has a structure-stabilizing role, which is supported by its inner structure [9] and its binding to chromatin remodeling factors such as EXPAND1 and PTIP [17,18]. The labeling of 53BP1 IRIF through immunofluorescence is used together with γ H2AX as a dosimetry measure of low-LET radiation via the foci assay. But also in studies related to chromatin and DNA repair structure, 53BP1 plays a major role [9,10,19,20]. For example, the co-staining of 53BP1 and Rad51 showed a local exclusion at the DSB location in super-resolution STED images. Recent studies conclude that by labeling Rad51, the damage itself can be labeled; 53BP1 labels the active repair region containing the relevant proteins, and γ H2AX marks the decondensed DNA surrounding the damage [9,10,20].

In recent years, it turned out that DSB repair not only depends on the cell cycle state and damage complexity but also on the location of the DSB in the cell nucleus [21,22]. Moreover, the functional and structural chromatin organization, its dynamic reorganization upon DSB induction, and its regulative influence on DNA repair define the type and efficiency of repair [23–27]. A well-accepted model of chromatin organization is the chromosome territory interchromatin compartment (CT-IC) model. This model is based on various microscopic studies on the distribution of different chromosomes in the cell nucleus. The chromatin in the interphase is divided into so-called chromatin domains, which correspond to the single chromosomes containing a substructure. In this substructure, three areas are defined: the chromatin territories (CTs), the interchromatin compartment (IC), and the perichromatin (PR) [28,29]. The CTs contain condensed DNA of the chromosome, which is densely packed and therefore thereby protected from toxic agents, such as reactive species. Additionally, the CT is a highly dynamic structure, as throughout the cell cycle, various regions need to be accessed by proteins, e.g., for transcription [30]. It is not yet known whether this dynamic change is due to Brownian motion or occurs through a directed movement dependent on actin, tubulin, or ATP [31,32]. In between the CTs, there are DNA-free regions connected by DNA-free channels called interchromatin compartments (ICs). The ICs are responsible for material and protein transport to varying gene loci as well as buffer storage of proteins and substrates [31]. The majority of proteins located in the IC are part of the posttranslational splicing apparatus. One of these proteins is the splicing protein SC35, which is part of the serin–arginine splicing factor (SR) family. It contains 303 amino acids and, through a highly conserved RNA-binding domain, is responsible for the processing of transcription products in the cell nucleus. It frequently occurs in the cell nucleus and is distributed in the whole IC through so-called speckles [33,34]. This location makes SC35 a perfect candidate for labeling and imaging the IC through fluorescence microscopy. The CT and the IC are separated by a <200 nm thick region called the perichromatin (PR) [9,28]. This boundary layer contains loosened DNA with active gene expression or actively repaired DNA regions. Furthermore, it is assumed that this region contains actively transcribed DNA parts in so-called transcription loops with a

length of ~200 nm [35,36]. This model supports DNA mobility, which is necessary to bring transcription proteins and gene loci in the PR together. However, in this model, it is not necessary to transport a defined gene locus to a distant transcription site all across the cell nucleus. Also, from this point of view, the CT-IC model seems to be more realistic. For efficient DNA repair, the accessibility of the damaged region also plays a major role. Moreover, the detailed structure of the DNA at the time of repair is important to support proper repair and decrease the probability of mis- or un-joined DNA ends [37]. The accumulation of DNA repair proteins at the damaged DNA locus is highly dependent on the accessibility of the damage. However, the detailed structure and dynamics of DNA organization upon damage induction are not yet known and are part of ongoing research worldwide. The focus of this study lies in the identification of the chromatin structure surrounding damage induced by high-LET carbon ions to be able to clarify the connection between DNA damage location and efficiency of repair. The overlap between the IC, CT, PR, and the damage location is analyzed using immunofluorescence super-resolution microscopy. This leads to an enhanced model of chromatin organization after DNA damage induction.

2. Results

In this study, the complex connection between chromatin organization and DSB repair is revealed by analyzing the overlap between different chromatin structures and repair proteins using a software-based pixel-wise analysis, developed as a plugin for ImageJ (Version 1.52n), of single slices of 3D image stacks. For each combination, 50 cells from three independent experiments with three samples each were analyzed. All errors represent the standard error of the mean. Quantitative results can be found in Table 1.

Table 1. Overlapping regions in the various combinations of staining for irradiated regions in all cases except SC35 + Chromatin, where random regions within the cell nuclei were chosen.

| Combination | Overlap % |
|-------------------------|-----------|
| SC35 + Chromatin | 29 ± 9 |
| 53BP1 + Chromatin | 38 ± 14 |
| Rad51 + Chromatin | 60 ± 15 |
| Rad51 + Heterochromatin | 10 ± 2 |
| 53BP1 + SC35 | 1.0 ± 0.2 |
| Rad51 + γ H2AX | 36 ± 15 |

The comparison of chromatin and interchromatin was performed by comparing the DNA label with the SC35 splicing factor. SC35 shows speckle-like structures in the regions with low DNA staining intensity (Figure 1a). The channels of the IC containing SC35 pervade the chromatin through the whole cell nucleus. Quantitative correlation analysis shows that (29 ± 9)% of the SC35-positive regions overlap with chromatin. This overlap is located in the border region between the two analyzed structures. By reducing the chromatin signal to the visible connections, which was performed using the skeletonize tool from ImageJ as described in the Section 4, the complex chromatin network can be visualized and the chromatin branches and their overlap with other labeled structures can be measured. The chromatin merely passes by the SC35 positive regions, and only a few ends touch the edges of the SC35 label.

In the next step, the overlap between the DNA repair region, labeled by 53BP1, and the chromatin was analyzed (cf. Figure 1b). Here again, the complex chromatin structure is visible. Furthermore, there is a visible overlap at the border of the 53BP1 foci and where single chromatin branches extend into the 53BP1-positive region. Overall, the quantitative analysis shows that (38 ± 14)% of the 53BP1-positive region overlaps with chromatin.

Next, the location of interchromatin, represented by SC35, and the region of active DSB repair, labeled by 53BP1, were compared, as shown in Figure 2a. Here, mutual exclusion is found, and only $(1 \pm 0.2)\%$ of the 53BP1-positive region shows overlap with the SC35-positive region. Moreover, a buffer zone between the two signals is visible in the analysis, which could be quantified as surrounding a total amount of 134 53BP1 foci to (270 ± 40) nm thickness. This was determined by drawing an intensity profile between the two structures (53BP1 focus and SC35 signal) perpendicular to the surface of the 53BP1 focus and fitting a Gaussian function to the resulting profile (see Figure 2b). The full width at half maximum corresponds to the width of the gap.

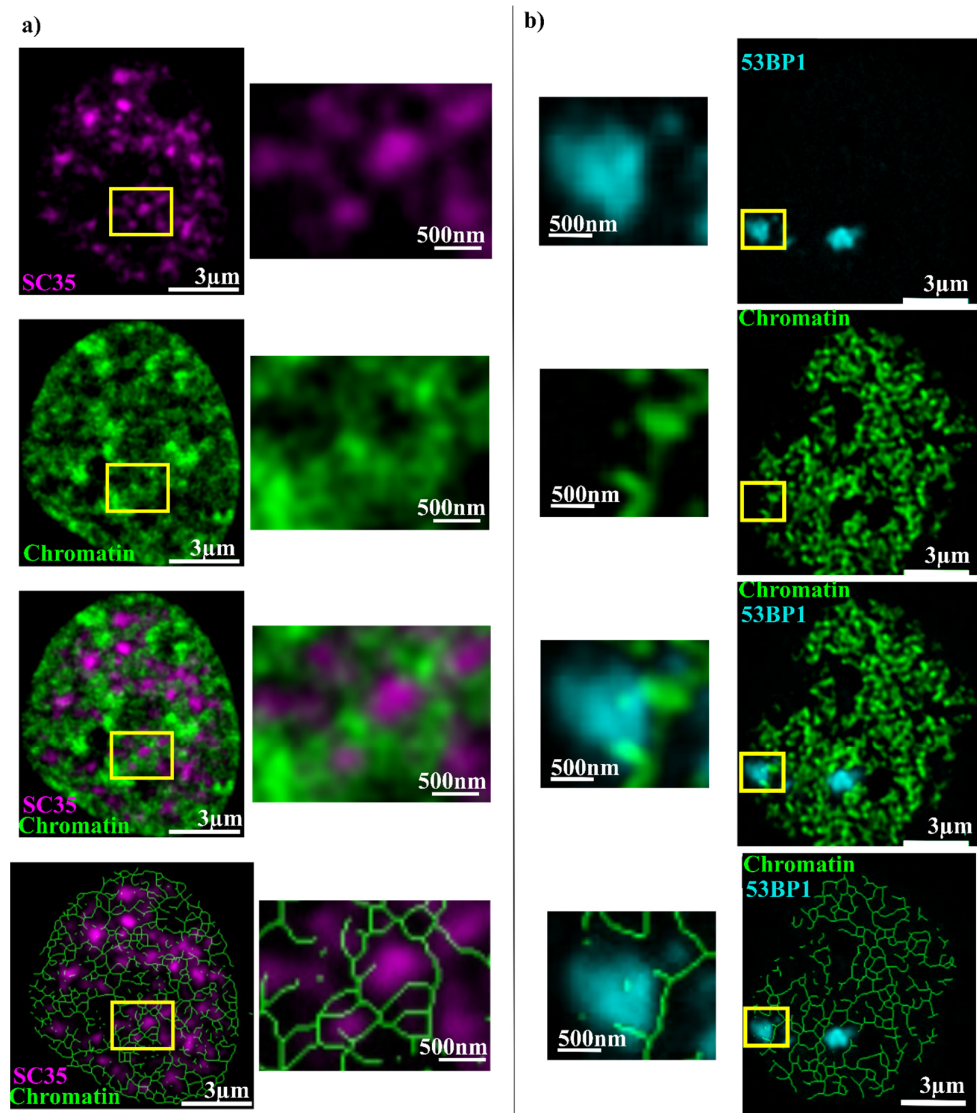


Figure 1. (a) HeLa cell with labeled chromatin (green) and SC35 (magenta) as an interchromatin marker. The first row shows SC35, the second row chromatin, the third row the overlay, and the fourth row the chromatin network together with SC35. The right column shows a zoom of the yellow box. (b) HeLa cell with labeled chromatin (green) and 53BP1 (cyan). The first row shows 53BP1, the second row chromatin, the third row the overlay, and the fourth row the chromatin network together with 53BP1. The chromatin network was achieved by using the skeletonize tool from ImageJ on the signal above the threshold used also for correlation analysis. The left column shows a zoom of the yellow box. No threshold is used for the image data shown.

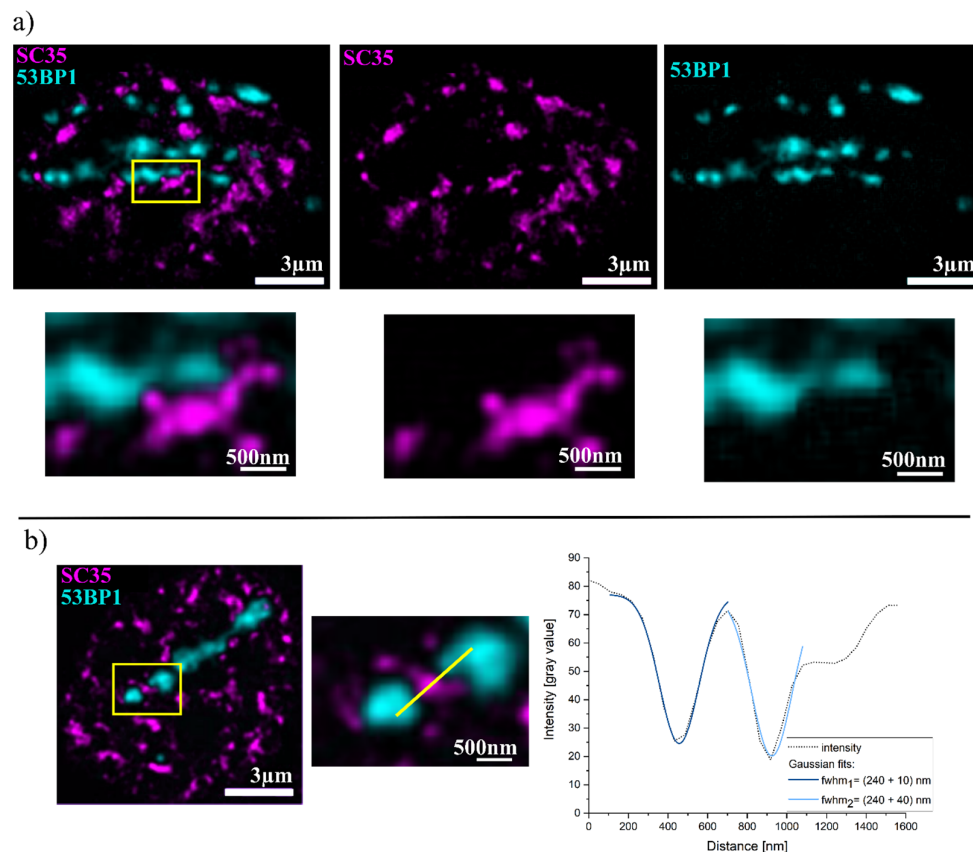


Figure 2. (a) HeLa cells with SC35 interchromatin labeling (magenta) and 53BP1 labeling of carbon-ion-induced damage (cyan). The first column shows the overlay, and the second and third columns show SC35 and 53BP1, respectively. The second line shows the zoom of the yellow box. (b) Example analysis of the buffer zone. IRIFs are enlarged, and a line is drawn between 53BP1 and SC35, perpendicular to the 53BP1 signal surface. The figure shows the analysis of two separate buffer zones within the ROI. The intensity profile is shown on the right. The two dips in intensity were analyzed using a Gaussian fit. No threshold was used for the image data shown.

Additionally, the connection between Rad51, which is labeling the location of the DSBs, and the chromatin was analyzed (Figure 3a). Here, an overlap of $(60 \pm 15)\%$ was visible. Heterochromatin isolation, as described in the materials and methods section, enables a more detailed analysis. It was revealed that Rad51 is not located in the heterochromatic regions, as it lies in the regions with low chromatin density, visible by low intensities in the SiR-DNA signal. Furthermore, the Rad51 foci are located at the edges of these regions, which seem to border the chromatin-rich heterochromatic regions. Overall, only $(10 \pm 2)\%$ of the Rad51 signal overlaps with heterochromatin, and the rest is lying in the euchromatin. Finally, Rad51 was correlated with γ H2AX (Figure 3b), which labels the DNA surrounding the DSB. Again, a partial overlap with $(36 \pm 15)\%$ between Rad51 and γ H2AX was measured.

To complete the analysis, size measurements of the overlap between the region surrounding the damage labeled by 53BP1 and the chromatin, as well as the Rad51 IRIF, were performed in 100 overlapping regions of each IRIF. The mean size of the Rad51 IRIF was $(0.12 \pm 0.05) \mu\text{m}^2$, whereas the overlapping regions were $(0.11 \pm 0.07) \mu\text{m}^2$.

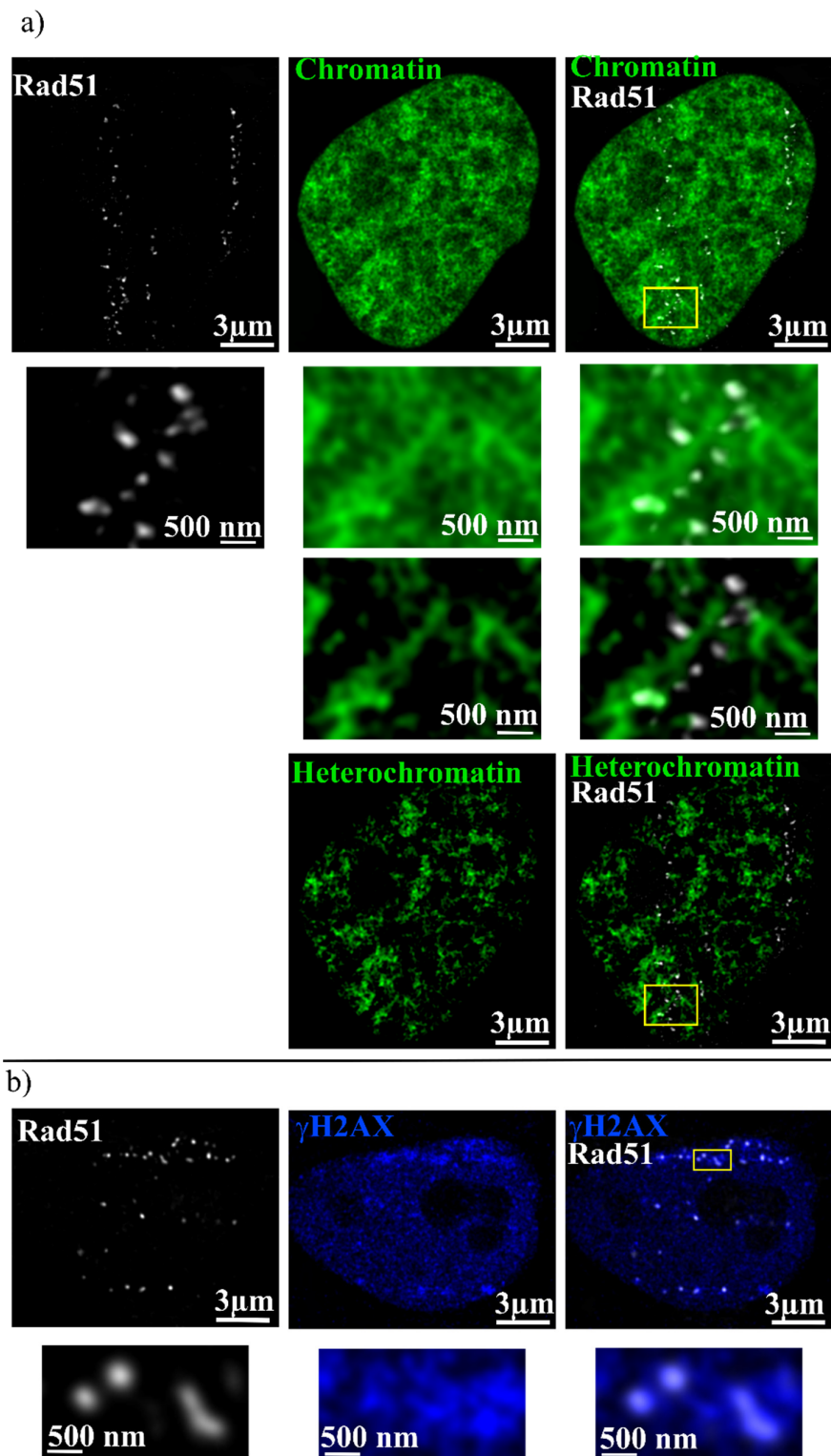


Figure 3. (a) Irradiated HeLa cell with chromatin (green) and Rad51 (gray) labeling. The first column shows Rad51, the second chromatin, and the third the overlay. The second row shows a zoom of the yellow box. In the two next rows, only the isolated heterochromatin of the same cell in combination with Rad51 is shown. (b) Irradiated HeLa cell showing Rad51 (gray) and γ H2AX (blue). The first column shows Rad51, the second γ H2AX, and the third the overlay. The lower row shows the zoom of the yellow box. No threshold is used for the image data shown.

3. Discussion

In this short study, we quantified the overlap of different active regions in the cell nucleus after irradiation with high-LET carbon ions in a pixel-wise analysis of separate slices of 3D image stacks. The aim was to provide additional input to the model of chromatin organization after damage induction and to expand the view of chromatin remodeling.

First of all, we could show that there is a high amount of interchromatin in the cell nucleus, which is in good correspondence with studies by Rouquette et al. [38]. The analysis of SC35 as an interchromatin marker and 53BP1 as a marker for the damaged region, as well as the analysis of interchromatin and chromatin, reveal a complex network of ICs and CTs formed in the cells, exhibiting a 270 nm wide margin of loosened chromatin, which is much larger than the resolution of 105 nm. These results nicely fit a model proposed by Cremer et al. [29,39,40], where an additional region, called perichromatin, is visible in the cells. This region is meant to contain relaxed DNA accessible for transcription, replication, or repair. It is located in the periphery of the chromatin territories. In our study, Rad51 is used as a DSB marker. This is valid, as it clusters to single-stranded DNA and is responsible for homology search during repair [41–43]. We could show that almost no Rad51 could be found in chromatin-rich regions but rather at its border. About 90% of all overlap between Rad51 and the DNA is in regions with low DNA density and, more importantly, not in the heterochromatin, as quantified by heterochromatin reduction together with overlap analysis. Furthermore, a clear overlap between Rad51 and DNA surrounding the damage is visible, as quantified by the partial overlap with γ H2AX. In correspondence with Albiez et al. [30], it can be assumed that the part of the Rad51 IRIF that does not overlap with DNA is responsible for assuring proper Rad51 supply at the damage itself.

The data, together with the existing literature about the models of chromatin organization [9,25,29,30,39,40,44], allow us to hypothesize the following model, which is also shown in Figure 4: The DNA surrounding the damage is loosened upon damage induction and recognition. This structure is supported by the phosphorylation of H2AX and the accumulation of 53BP1. For damage repair, the decondensed chromatin is stabilized as perichromatin. The DNA repair happens in the direct vicinity of the location of induction. The model of local chromatin reorganization is also supported by the fact that the visible damage track is not a straight line of IRIF, neither after ion-induced damage, as used here, nor after laser-induced damage [45,46]. An explanation of this can be that different chromatin densities influence the activation of γ H2AX and the accumulation of 53BP1. Therefore, a slightly waved track occurs. The exclusion of 53BP1 and SC35 as interchromatin markers supports the hypothesis of mechanical stabilization of the damage by the accumulation of DNA recognition and repair markers [9,10,47]. The overlap of 53BP1 with single, protruding chromatin branches gives rise to the assumption that these branches contain the DSB. Also, the good correspondence of the size of the overlapping regions of 53BP1 with chromatin branches and the size of the Rad51 IRIF, which both are approximately $0.1 \mu\text{m}^2$, support this conclusion. The processing of the DSB by CtIP and Rif1 does not require this large amount of 53BP1 in such a large region surrounding the damage [48]. Our results, therefore, support the stabilizing function of 53BP1 during damage repair, as found in other studies [9,10,20]. A further protective role can be assumed by looking at the mutual exclusion of 53BP1 and SC35. From the literature, it is known that no splicing factors may interact with the damage [49,50]. The accumulation of 53BP1 in a large region and the consecutive formation of a large perichromatin surrounding the damage may help to ensure proper DNA repair without the interference of noxious proteins and factors. Future studies should evaluate the role of 53BP1 in this protective function, as well as the function and composition of the 270 nm buffer zone. All results were obtained by analyzing individual slices of 3D image stacks. In principle, the use of 2D slices separately rather than using the 3D structure as a whole could affect the results, but the size identified is well above the lateral and axial resolution. Therefore, we conclude that the 2D analysis does not change the results.

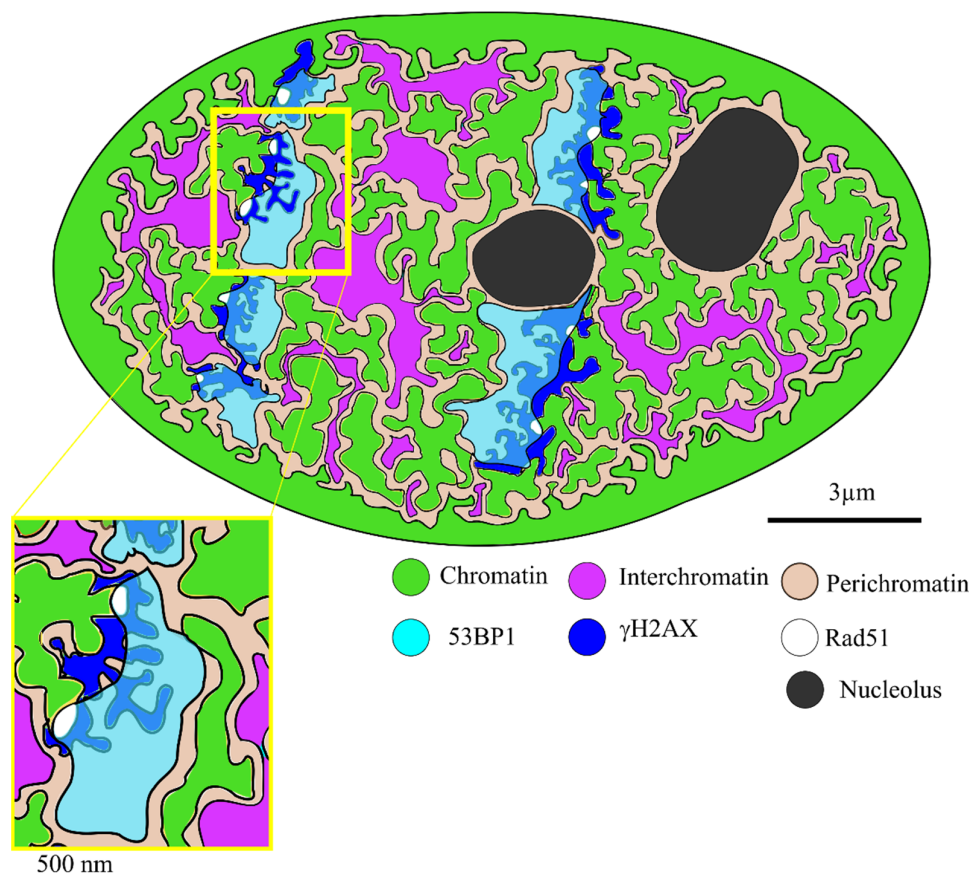


Figure 4. Schematic model of chromatin organization in a cell irradiated with high-LET particles. It is based on the conclusions drawn from this study and already accepted models of chromatin organization.

To sum up, it can be assumed that the DNA damage is repaired in decondensed DNA loops in the perichromatin, located in the periphery of the DNA-dense chromatin compartments. Proteins such as γ H2AX and 53BP1 mechanically support the structure and protect the regions from harmful interference. This allows the processing of the damage and the sensitive single-stranded DNA in the perichromatin and helps to assure error-free DSB repair.

One challenge with this type of analysis is the limited resolution of microscopy, which limits the structures that can be analyzed by different methods. In this study, we used 3D STED microscopy, which has a lateral resolution of 105 nm, well above the measured structure sizes of interest here. Other studies using STORM imaging have even identified substructures in the radiation-induced γ H2AX foci, called nanofoci, with smaller sizes down to tens of nanometers [51–54]. Although we were not able to resolve these nanofoci in this study, we believe that their existence points to another level of spatial arrangement, which is related to the way H2AX is incorporated into nucleosomes [52] and to the phosphorylation status upon damage induction [53,54], which we were not aiming to investigate here.

The growing understanding of the connection between the location of the DNA damage and the efficiency of repair mediated by chromatin structure and protein clustering helps to better understand DNA repair and radiation-induced disease patterns. In future studies, it would be interesting to add more proteins related to DNA repair into this localization picture; this would be even more interesting in other cell lines, such as fibroblasts or other tumor types. Furthermore, the temporal component is not yet well understood or investigated. For these types of studies, it would be of great interest to develop a suited live-cell model for super-resolution STED microscopy with multicolor samples.

4. Materials and Methods

4.1. Cell Culture and Irradiation

Culture of the HeLa cells (courtesy of AG Friedl, LMU Munich, Germany) was performed in an incubator at 37 °C (100% humidity, 95% air + 5% CO₂) using RPMI medium (Sigma-Aldrich, St. Louis, Missouri, USA) containing 10% FCS and 1% penicillin/streptomycin as described previously [9]. For irradiation, 400,000 cells were seeded on (22 × 22) mm² coverslips and placed in 6-well plates together with 2 mL medium on the previous day. Therefore, cells were in the exponential growth phase at the time of irradiation with 55 MeV carbon ions at the microirradiation facility SNAKE [55]. The irradiation procedure in total lasted 20 s. To keep the sample from drying, a thin layer of medium was kept on top of the cell layer. It had a thickness of $d = (7.5 \pm 2.5) \mu\text{m}$, which was determined by weight measurements and calculation through the formula $d = \frac{m}{A \times \rho_{\text{water}}}$, where m is the mass, $A = (22 \times 22) \text{mm}^2$ is the area of the coverslip, and the density of water is $\rho_{\text{water}} = 1 \frac{\text{g}}{\text{cm}^3}$. To obtain the defined medium thickness, the sample was taken out of the medium one minute before irradiation and dried carefully in air. The air gap between the beam exit nozzle and the sample, as well as the medium layer, caused energy loss. This led to ion energy at the cell surface of $(27 \pm 8) \text{MeV}$ and a linear energy transfer (LET) of $\text{LET} = (500 \pm 80) \text{keV}/\mu\text{m}$. Irradiation was performed in a field of $(3.5 \times 22) \text{mm}^2$ under an angle of 9° concerning the cell layer and lasted a few seconds. The fluence of the carbon ion beam was $F = \frac{0.03}{\mu\text{m}^2}$ with a variation of 20% due to ion count rate fluctuations, which led to a dose of: $D = \frac{F \times \text{LET}}{\rho_{\text{water}}} = (2.4 \pm 0.6) \text{Gy}$. Per cell nucleus, there were typically two to three ion traversals visible.

4.2. Antibodies and Immunofluorescence Detection

After irradiation, samples were placed back in the 6-well and incubated for 1 h in the incubator. After the incubation time, cells were fixed for 15 min in a 2% (*w/v*) paraformaldehyde solution in PBS. This was followed by washing two times with phosphate-buffered saline (PBS), and performing three rounds of permeabilization for 5 min each with a 0.15% (*v/v*) Triton-X-100 solution in PBS. Then, the cells were blocked three times with PBS containing 1% bovine serum albumin (BSA) and 0.15% glycine for 10 min each, as previously described by Reindl et al. [9]. The labeling was performed with mouse anti-γH2AX (m-a-γH2AX, Sigma Aldrich, Burlington, MA, USA, #05-636, 1:350), rabbit anti-53BP1 (r-a-53BP1, Novus biologicals, BioTechne, Minneapolis, MN, USA, #NB100-305, 1:350), mouse anti-Rad51 (m-a-Rad51, GeneTex Irvine, CA, USA, #GTX70230, 1:350), or mouse anti-SC35 (m-a-SC35, Abcam, Cambridge, UK, #ab11826, 1:350) primary antibody. Samples with primary antibodies were incubated in a humid chamber at 4 °C overnight. After incubation, the samples were washed with PBS, permeabilized with Triton-X-100 for 5 min, and blocked with PBS containing BSA and glycine for 10 min. After this, the secondary antibodies were added: goat-anti-mouse or goat-anti-rabbit Alexa 488 (gam-Alexa 488 and gar-Alexa 488, ThermoFisher Scientific, Waltham, MA, USA, #A-11001 and #A-11034, 1:500) and goat-anti-rabbit Alexa 532 (gar-Alexa 532, ThermoFisher Scientific, Waltham, MA, USA #A-11009, 1:500). The samples were incubated with antibodies in a humid chamber for 2 h at room temperature. After this final incubation step, samples were washed carefully several times and mounted on glass slides using ProLong Diamond (Sigma Aldrich, Burlington, MA, USA) mounting medium. After 48 h of drying at room temperature under light exclusion, the slides were imaged and stored at 4 °C. For chromatin labeling, cells were labeled using a far-red SiR-DNA Kit (Spiochrome, Stein am Rhein, Germany). For labeling, the medium was exchanged just before irradiation and replaced with a 1000 nM solution of the Kit diluted in the medium. For the experiments, five types of co-staining were used, as shown in Table 2.

Table 2. Staining combinations used in this study.

| Co-Staining | Dye 1 | Dye 2 |
|--------------------------------|---------------|---------------|
| m-a-SC35 + SiR-DNA | gar-Alexa 488 | SiR 650 |
| r-a-53BP1 + SiR-DNA | gar-Alexa 488 | SiR 650 |
| m-a-SC35 + r-a-53BP1 | gam-Alexa 488 | gar-Alexa 532 |
| r-a-Rad51 + SiR-DNA | gar-Alexa 488 | SiR 650 |
| r-a-Rad51 + m-a- γ H2AX | gam-Alexa 488 | gar-Alexa 532 |

4.3. Microscopy

For imaging, a super-resolution optical CW STED microscope (Leica TCS SP 8 3X) was used. Excitation wavelengths 470 nm for the Abberior STAR 440SX, 514 nm for Chromeo505, and 640 nm for the SiR-DNA dye were set. The detection ranges were 473 nm to 504 nm and 518 nm to 580 nm, respectively, with a depletion laser at 592 nm for the antibodies and 650 nm to 700 nm with a STED laser at 775 nm for the SiR-DNA dye. Laser power for the excitation laser was on the order of 1 mW, and that for the STED lasers was approximately 70 mW. The STED lasers were subdivided into a lateral STED beam (40% of the energy) and an axial STED beam (60%). The temporal and temperature-dependent shift was excluded, as described previously [19]. Stacks of cell nuclei (3–5 μ m thickness) with a slice distance of 160 nm were acquired with a 100x oil objective (Leica HCX PL APO 100x/1.4 Oil) and a pixel size of 40 nm. The raw data images were deconvolved using Huygens Professional (Scientific Volume Imaging, Hilversum, Netherlands) as described previously [19], resulting in a lateral resolution of 105 nm and an axial resolution of 200 nm.

4.4. Heterochromatin Isolation

Heterochromatin was isolated according to the value defined by Imai et al. [56]. Here, all chromatin regions were euchromatin, which has an intensity value below the threshold of $T = \frac{I_{max}}{(6.5 \pm 1.0)}$, where I_{max} is the maximum intensity of chromatin visible in the image. Therefore, in each image, the maximum intensity was determined, and all signals were neglected below the threshold. The residual signal was considered to represent heterochromatin.

4.5. Overlap Analysis

For overlap analysis, the reduced product of the differences from the mean (rPDM) analysis was used for the separate slices of the 3D image stacks as described in detail by Reindl et al. [19]. This analysis is available as an ImageJ (<https://imagej.net/ij/> (accessed on 27 November 2023)) software plugin for free use. Briefly, a threshold is determined above which the pixels are included for analysis. The area to be analyzed is cut out with a large margin. Then, the area of the region with a signal above a certain gray value is determined. This is performed for a range of gray values. Then the areas are compared, and a range of gray values is selected where the change in the size of the area is small in relation to the change in the gray value; i.e., a 20% change in the gray value results in a maximum 10% change in the area. After this, the rPDM value is calculated for each pixel using the following formula:

$$rPDM = \begin{cases} d, & |R_i < R_{mean} \wedge G_i < G_{mean} \\ \frac{(R_i - R_{mean})(G_i - G_{mean})}{(R_{max} - R_{mean})(G_{max} - G_{mean})}, & x \geq 0 \end{cases}$$

where $d \in \mathbb{R} \setminus [-1, 1]$; R_i and G_i are the pixel values of the two channels; and R_{mean} , G_{mean} , R_{max} , G_{max} are the corresponding mean and maximum values. For overlap analysis, only pixels are considered that have higher pixel values than the mean in both channels. Here, two groups of pixels occur. The first groups are pixels with negative rPDM, where only one channel has a high signal; therefore, no overlap is visible. The second group with positive rPDM is the overlapping group, as there is high signal intensity in both channels. To obtain

the fraction of overlapping pixels F_O , the number of pixels with positive rPDM, P_{pos} , is divided by the total number of pixels, $P_{tot, channel}$, in the relevant channel: $F_O = \frac{P_{pos}}{P_{tot, channel}}$. The analysis was performed on irradiated samples in all cases. In the analysis of SC35 together with chromatin staining, the irradiated region within the cells was not clearly visible. Therefore, random positions within the cell nuclei were chosen.

4.6. Distillation of Chromatin Network

The chromatin network was achieved by using the skeletonize tool from ImageJ software. This tool is based on the work by Lee et al. [57]. With this tool, the centerlines of the underlying network are determined in the analyzed images. For this, binary images are used, where all signals above the threshold determined for the correlation analysis are set to 255 and all other signals are set to 0. The skeletonizing is applied to these binary images, as automatically implemented in ImageJ. The remaining skeleton is considered the chromatin network.

Author Contributions: Conceptualization, B.S. and J.R.; methodology, B.S. and J.R.; software, J.R.; validation, B.S., J.R., N.M., S.R. and M.S.; formal analysis, B.S.; investigation, B.S., N.M., S.R. and M.S.; resources, J.R.; data curation, B.S. and J.R.; writing—original draft preparation, J.R. and B.S.; writing—review and editing, N.M., S.R. and M.S.; visualization, B.S.; supervision, J.R.; project administration, J.R. All authors have read and agreed to the published version of the manuscript.

Funding: This research received no external funding.

Institutional Review Board Statement: Not applicable.

Informed Consent Statement: Not applicable.

Data Availability Statement: The data presented in this study are available on request from the corresponding author. The data are not publicly available due to restriction of the university.

Conflicts of Interest: The authors declare no conflicts of interest.

References

- Rothkamm, K.; Barnard, S.; Moquet, J.; Ellender, M.; Rana, Z.; Burdak-Rothkamm, S. DNA damage foci: Meaning and significance. *Environ. Mol. Mutagen.* **2015**, *56*, 491–504. [[CrossRef](#)]
- Natarajan, A.T.; Palitti, F. DNA repair and chromosomal alterations. *Mutat. Res.* **2008**, *657*, 3–7. [[CrossRef](#)] [[PubMed](#)]
- Pardo, B.; Gómez-González, B.; Aguilera, A. DNA repair in mammalian cells: DNA double-strand break repair: How to fix a broken relationship. *Cell. Mol. Life Sci.* **2009**, *66*, 1039–1056. [[CrossRef](#)]
- Shibata, A.; Conrad, S.; Birraux, J.; Geuting, V.; Barton, O.; Ismail, A.; Kakarougkas, A.; Meek, K.; Taucher-Scholz, G.; Löbrich, M.; et al. Factors determining DNA double-strand break repair pathway choice in G2 phase. *EMBO J.* **2011**, *30*, 1079–1092. [[CrossRef](#)] [[PubMed](#)]
- Schipler, A.; Iliakis, G. DNA double-strand-break complexity levels and their possible contributions to the probability for error-prone processing and repair pathway choice. *Nucleic Acids Res.* **2013**, *41*, 7589–7605. [[CrossRef](#)] [[PubMed](#)]
- Rothkamm, K.; Krüger, I.; Thompson, L.H.; Löbrich, M. Pathways of DNA double-strand break repair during the mammalian cell cycle. *Mol. Cell. Biol.* **2003**, *23*, 5706–5715. [[CrossRef](#)] [[PubMed](#)]
- Baumann, P.; West, S.C. Role of the human RAD51 protein in homologous recombination and double-stranded-break repair. *Trends Biochem. Sci.* **1998**, *23*, 247–251. [[CrossRef](#)] [[PubMed](#)]
- Sung, P.; Krejci, L.; van Komen, S.; Sehorn, M.G. Rad51 recombinase and recombination mediators. *J. Biol. Chem.* **2003**, *278*, 42729–42732. [[CrossRef](#)]
- Reindl, J.; Girst, S.; Walsh, D.W.M.; Greubel, C.; Schwarz, B.; Siebenwirth, C.; Drexler, G.A.; Friedl, A.A.; Dollinger, G. Chromatin organization revealed by nanostructure of irradiation induced γ H2AX, 53BP1 and Rad51 foci. *Sci. Rep.* **2017**, *7*, 40616. [[CrossRef](#)]
- Schwarz, B.; Friedl, A.A.; Girst, S.; Dollinger, G.; Reindl, J. Nanoscopic analysis of 53BP1, BRCA1 and Rad51 reveals new insights in temporal progression of DNA-repair and pathway choice. *Mutat. Res.* **2019**, *816–818*, 111675. [[CrossRef](#)]
- Adams, M.M.; Carpenter, P.B. Tying the loose ends together in DNA double strand break repair with 53BP1. *Cell Div.* **2006**, *1*, 19. [[CrossRef](#)] [[PubMed](#)]
- Lee, H.; Kwak, H.-J.; Cho, I.-t.; Park, S.H.; Lee, C.-H. S1219 residue of 53BP1 is phosphorylated by ATM kinase upon DNA damage and required for proper execution of DNA damage response. *Biochem. Biophys. Res. Commun.* **2009**, *378*, 32–36. [[CrossRef](#)] [[PubMed](#)]

13. Hable, V.; Drexler, G.A.; Brüning, T.; Burgdorf, C.; Greubel, C.; Derer, A.; Seel, J.; Strickfaden, H.; Cremer, T.; Friedl, A.A.; et al. Recruitment kinetics of DNA repair proteins Mdc1 and Rad52 but not 53BP1 depend on damage complexity. *PLoS ONE* **2012**, *7*, e41943. [[CrossRef](#)] [[PubMed](#)]
14. Feng, L.; Fong, K.-W.; Wang, J.; Wang, W.; Chen, J. RIF1 counteracts BRCA1-mediated end resection during DNA repair. *J. Biol. Chem.* **2013**, *288*, 11135–11143. [[CrossRef](#)] [[PubMed](#)]
15. Gupta, A.; Hunt, C.R.; Chakraborty, S.; Pandita, R.K.; Yordy, J.; Ramnarain, D.B.; Horikoshi, N.; Pandita, T.K. Role of 53BP1 in the regulation of DNA double-strand break repair pathway choice. *Radiat. Res.* **2014**, *181*, 1–8. [[CrossRef](#)] [[PubMed](#)]
16. Zimmermann, M.; Lotterberger, F.; Buonomo, S.B.; Sfeir, A.; de Lange, T. 53BP1 regulates DSB repair using Rif1 to control 5' end resection. *Science* **2013**, *339*, 700–704. [[CrossRef](#)]
17. Huen, M.S.Y.; Huang, J.; Leung, J.W.C.; Sy, S.M.-H.; Leung, K.M.; Ching, Y.-P.; Tsao, S.W.; Chen, J. Regulation of chromatin architecture by the PWWP domain-containing DNA damage-responsive factor EXPAND1/MUM1. *Mol. Cell* **2010**, *37*, 854–864. [[CrossRef](#)]
18. Escribano-Diaz, C.; Durocher, D. DNA repair pathway choice—A PTIP of the hat to 53BP1. *EMBO Rep.* **2013**, *14*, 665–666. [[CrossRef](#)]
19. Reindl, J.; Drexler, G.A.; Girst, S.; Greubel, C.; Siebenwirth, C.; Drexler, S.E.; Dollinger, G.; Friedl, A.A. Nanoscopic exclusion between Rad51 and 53BP1 after ion irradiation in human HeLa cells. *Phys. Biol.* **2015**, *12*, 66005. [[CrossRef](#)]
20. Ochs, F.; Somyajit, K.; Altmeyer, M.; Rask, M.-B.; Lukas, J.; Lukas, C. 53BP1 fosters fidelity of homology-directed DNA repair. *Nat. Struct. Mol. Biol.* **2016**, *23*, 714–721. [[CrossRef](#)]
21. Klosin, A.; Hyman, A.A. Molecular biology: A liquid reservoir for silent chromatin. *Nature* **2017**, *547*, 168–170. [[CrossRef](#)] [[PubMed](#)]
22. Phipps, J.; Dubrana, K. DNA Repair in Space and Time: Safeguarding the Genome with the Cohesin Complex. *Genes* **2022**, *13*, 198. [[CrossRef](#)] [[PubMed](#)]
23. Lisby, M.; Mortensen, U.H.; Rothstein, R. Colocalization of multiple DNA double-strand breaks at a single Rad52 repair centre. *Nat. Cell Biol.* **2003**, *5*, 572–577. [[CrossRef](#)] [[PubMed](#)]
24. Caron, P.; Choudjaye, J.; Clouaire, T.; Bugler, B.; Daburon, V.; Aguirrebengoa, M.; Mangeat, T.; Iacovoni, J.S.; Álvarez-Quilón, A.; Cortés-Ledesma, F.; et al. Non-redundant Functions of ATM and DNA-PKcs in Response to DNA Double-Strand Breaks. *Cell Rep.* **2015**, *13*, 1598–1609. [[CrossRef](#)] [[PubMed](#)]
25. Ortega, P.; Gómez-González, B.; Aguilera, A. Heterogeneity of DNA damage incidence and repair in different chromatin contexts. *DNA Repair* **2021**, *107*, 103210. [[CrossRef](#)] [[PubMed](#)]
26. Yasuhara, T.; Zou, L. Impacts of chromatin dynamics and compartmentalization on DNA repair. *DNA Repair* **2021**, *105*, 103162. [[CrossRef](#)] [[PubMed](#)]
27. Minami, K.; Iida, S.; Maeshima, K. Chromatin organization and DNA damage. *Enzymes* **2022**, *51*, 29–51. [[CrossRef](#)] [[PubMed](#)]
28. Fakan, S.; van Driel, R. The perichromatin region: A functional compartment in the nucleus that determines large-scale chromatin folding. *Semin. Cell Dev. Biol.* **2007**, *18*, 676–681. [[CrossRef](#)]
29. Cremer, T.; Cremer, M. Chromosome territories. *Cold Spring Harb. Perspect. Biol.* **2010**, *2*, a003889. [[CrossRef](#)]
30. Albiez, H.; Cremer, M.; Tiberi, C.; Vecchio, L.; Schermelleh, L.; Dittrich, S.; Küpper, K.; Joffe, B.; Thormeyer, T.; von Hase, J.; et al. Chromatin domains and the interchromatin compartment form structurally defined and functionally interacting nuclear networks. *Chromosome Res.* **2006**, *14*, 707–733. [[CrossRef](#)]
31. Dion, V.; Gasser, S.M. Chromatin movement in the maintenance of genome stability. *Cell* **2013**, *152*, 1355–1364. [[CrossRef](#)] [[PubMed](#)]
32. Shinkai, S.; Nozaki, T.; Maeshima, K.; Togashi, Y. Dynamic Nucleosome Movement Provides Structural Information of Topological Chromatin Domains in Living Human Cells. *PLoS Comput. Biol.* **2016**, *12*, e1005136. [[CrossRef](#)] [[PubMed](#)]
33. Tacke, R.; Manley, J.L. The human splicing factors ASF/SF2 and SC35 possess distinct, functionally significant RNA binding specificities. *EMBO J.* **1995**, *14*, 3540–3551. [[CrossRef](#)] [[PubMed](#)]
34. Spector, D.L.; Lamond, A.I. Nuclear speckles. *Cold Spring Harb. Perspect. Biol.* **2011**, *3*, a000646. [[CrossRef](#)]
35. Fraser, P.; Bickmore, W. Nuclear organization of the genome and the potential for gene regulation. *Nature* **2007**, *447*, 413–417. [[CrossRef](#)]
36. Morgan, G.T. Imaging the dynamics of transcription loops in living chromosomes. *Chromosoma* **2018**, *127*, 361–374. [[CrossRef](#)]
37. Dabin, J.; Mori, M.; Polo, S.E. The DNA damage response in the chromatin context: A coordinated process. *Curr. Opin. Cell Biol.* **2023**, *82*, 102176. [[CrossRef](#)]
38. Rouquette, J.; Genoud, C.; Vazquez-Nin, G.H.; Kraus, B.; Cremer, T.; Fakan, S. Revealing the high-resolution three-dimensional network of chromatin and interchromatin space: A novel electron-microscopic approach to reconstructing nuclear architecture. *Chromosome Res.* **2009**, *17*, 801–810. [[CrossRef](#)]
39. Cremer, T.; Küpper, K.; Dietzel, S.; Fakan, S. Higher order chromatin architecture in the cell nucleus: On the way from structure to function. *Biol. Cell* **2004**, *96*, 555–567. [[CrossRef](#)]
40. Fakan, S. The functional architecture of the nucleus as analysed by ultrastructural cytochemistry. *Histochem. Cell Biol.* **2004**, *122*, 83–93. [[CrossRef](#)]
41. Barzel, A.; Kupiec, M. Finding a match: How do homologous sequences get together for recombination? *Nat. Rev. Genet.* **2008**, *9*, 27–37. [[CrossRef](#)]

42. Renkawitz, J.; Lademann, C.A.; Jentsch, S. Mechanisms and principles of homology search during recombination. *Nat. Rev. Mol. Cell Biol.* **2014**, *15*, 369–383. [[CrossRef](#)] [[PubMed](#)]
43. Greene, E.C. DNA Sequence Alignment during Homologous Recombination. *J. Biol. Chem.* **2016**, *291*, 11572–11580. [[CrossRef](#)] [[PubMed](#)]
44. Mersch, J.; Jackson, M.A.; Park, M.; Nebgen, D.; Peterson, S.K.; Singletary, C.; Arun, B.K.; Litton, J.K. Cancers associated with *BRCA1* and *BRCA2* mutations other than breast and ovarian. *Cancer* **2015**, *121*, 269–275. [[CrossRef](#)] [[PubMed](#)]
45. Marnef, A.; Legube, G. Organizing DNA repair in the nucleus: DSBs hit the road. *Curr. Opin. Cell Biol.* **2017**, *46*, 1–8. [[CrossRef](#)]
46. Jakob, B.; Splinter, J.; Conrad, S.; Voss, K.-O.; Zink, D.; Durante, M.; Löbrich, M.; Taucher-Scholz, G. DNA double-strand breaks in heterochromatin elicit fast repair protein recruitment, histone H2AX phosphorylation and relocation to euchromatin. *Nucleic Acids Res.* **2011**, *39*, 6489–6499. [[CrossRef](#)]
47. Guo, X.; Bai, Y.; Zhao, M.; Zhou, M.; Shen, Q.; Yun, C.-H.; Zhang, H.; Zhu, W.-G.; Wang, J. Acetylation of 53BP1 dictates the DNA double strand break repair pathway. *Nucleic Acids Res.* **2018**, *46*, 689–703. [[CrossRef](#)]
48. Xu, Y.; Ning, S.; Wei, Z.; Xu, R.; Xu, X.; Xing, M.; Guo, R.; Xu, D. 53BP1 and BRCA1 control pathway choice for stalled replication restart. *eLife* **2017**, *6*, e30523. [[CrossRef](#)]
49. Shanbhag, N.M.; Rafalska-Metcalf, I.U.; Balane-Bolivar, C.; Janicki, S.M.; Greenberg, R.A. ATM-dependent chromatin changes silence transcription in cis to DNA double-strand breaks. *Cell* **2010**, *141*, 970–981. [[CrossRef](#)]
50. Beli, P.; Lukashchuk, N.; Wagner, S.A.; Weinert, B.T.; Olsen, J.V.; Baskcomb, L.; Mann, M.; Jackson, S.P.; Choudhary, C. Proteomic investigations reveal a role for RNA processing factor THRAP3 in the DNA damage response. *Mol. Cell* **2012**, *46*, 212–225. [[CrossRef](#)]
51. Lopez Perez, R.; Best, G.; Nicolay, N.H.; Greubel, C.; Rossberger, S.; Reindl, J.; Dollinger, G.; Weber, K.-J.; Cremer, C.; Huber, P.E. Superresolution light microscopy shows nanostructure of carbon ion radiation-induced DNA double-strand break repair foci. *FASEB J.* **2016**, *30*, 2767–2776. [[CrossRef](#)] [[PubMed](#)]
52. Varga, D.; Majoros, H.; Ujfaludi, Z.; Erdélyi, M.; Pankotai, T. Quantification of DNA damage induced repair focus formation via super-resolution dSTORM localization microscopy. *Nanoscale* **2019**, *11*, 14226–14236. [[CrossRef](#)] [[PubMed](#)]
53. Liddle, P.; Jara-Wilde, J.; Lafon-Hughes, L.; Castro, I.; Härtel, S.; Folle, G. dSTORM microscopy evidences in HeLa cells clustered and scattered γ H2AX nanofoci sensitive to ATM, DNA-PK, and ATR kinase inhibitors. *Mol. Cell. Biochem.* **2020**, *473*, 77–91. [[CrossRef](#)] [[PubMed](#)]
54. Hausmann, M.; Wagner, E.; Lee, J.-H.; Schrock, G.; Schaufler, W.; Krufczik, M.; Papenfuß, F.; Port, M.; Bestvater, F.; Scherthan, H. Super-resolution localization microscopy of radiation-induced histone H2AX-phosphorylation in relation to H3K9-trimethylation in HeLa cells. *Nanoscale* **2018**, *10*, 4320–4331. [[CrossRef](#)]
55. Hauptner, A.; Dietzel, S.; Drexler, G.A.; Reichart, P.; Krücken, R.; Cremer, T.; Friedl, A.A.; Dollinger, G. Microirradiation of cells with energetic heavy ions. *Radiat. Environ. Biophys.* **2004**, *42*, 237–245. [[CrossRef](#)]
56. Imai, R.; Nozaki, T.; Tani, T.; Kaizu, K.; Hibino, K.; Ide, S.; Tamura, S.; Takahashi, K.; Shribak, M.; Maeshima, K. Density imaging of heterochromatin in live cells using orientation-independent-DIC microscopy. *Mol. Biol. Cell* **2017**, *28*, 3349–3359. [[CrossRef](#)]
57. Lee, T.C.; Kashyap, R.L.; Chu, C.N. Building Skeleton Models via 3-D Medial Surface Axis Thinning Algorithms. *CVGIP Graph. Models Image Process.* **1994**, *56*, 462–478. [[CrossRef](#)]

Disclaimer/Publisher’s Note: The statements, opinions and data contained in all publications are solely those of the individual author(s) and contributor(s) and not of MDPI and/or the editor(s). MDPI and/or the editor(s) disclaim responsibility for any injury to people or property resulting from any ideas, methods, instructions or products referred to in the content.